Unveiling the galaxy population at $1.3 < z < 4$: the HUDF05 NICMOS Parallel Fields

Sara M. Petty,[1,2,3] Duília F. de Mello,[1,2] Tommy Wiklind,[4,5] Jonathan P. Gardner,[2] C. Matt Mountain[4]

ABSTRACT

Using the Hubble Ultra Deep Field Near Infrared Camera and Multi-Object Spectrometer (HUDF-NICMOS) UDF05 parallel fields, we cross-matched 301 out of 630 galaxies with the ACS filters V_{606} and z_{850}, NICMOS filters J_{110} and H_{160}, and Spitzer IRAC filters at 3.6, 4.5, 5.8 , and 8.0 μm. We modeled the spectral energy distributions (SEDs) to estimate: photometric redshifts, dust extinction, stellar mass, bolometric luminosity, starburst age and metallicity. To validate the photometric redshifts, comparisons with 16 spectroscopic redshifts give 75% within $\Delta \leq 0.2$, which agrees with the sensitivities expected from the Balmer-break in our dataset. Five parallel fields observed by NICMOS have sensitivities in the H_{160}-band of 80% at $m_{AB} = 25.4$ and 50% at $m_{AB} = 26.7$. Because the sample is H_{160}-band selected, it is sensitive to stellar mass rather than UV luminosities. We also use Monte Carlo simulations to determine that the parameters from the best-fit SEDs are robust for the redshift ranges $z \gtrsim 1.3$. Based on the robustness of the photometric redshifts, we analyze a subsample of the 301 galaxies at $1.3 \leq z \leq 2$ (35 objects) and $3 \leq z \leq 4$ (31 objects) and determine that L_{Bol} and the star formation rate increase significantly from $z \sim 1.5$ to 4. The Balmer decrement is indicative of more evolved galaxies, and at high redshifts, they serve as records of some of the first galaxies. Therefore, the galaxies in this sample are great candidates for future surveys with the James Webb Space Telescope and Atacama Large Millimeter Array.

Subject headings: cosmology: observations – galaxies: evolution – galaxies: high-redshift – galaxies: photometry

1. Introduction

As deeper infrared surveys have become available, the ability to detect fainter galaxies with prominent spectral features in the rest-frame optical is proving an important key in the evolution of the early universe to the present epoch. Multiple wavelength photometry (optical-infrared) is often used to determine the properties of high redshift galaxies, such as star formation rates, stellar mass and bolometric luminosity from inferences of nearby observations. The physical properties of nearby galaxies fit along the Hubble Sequence when observed in optical wavelengths. These properties often correlate with gas and dust content, star formation rates, ages and luminosities. At around $z \sim 1$ this classification scheme quickly fails. The relevance of using the known properties of nearby galaxies to compare with high redshift galaxies has been revisited many times showing that certain characteristics may be compared directly (e.g., Weedman & Huenemoerder 1985; Hibbard & Vacca 1997; Heckman et al. 2005; Lotz et al. 2006; Overzier et al. 2008; Petty et al. 2009; Overzier et al. 2010).

[1]Department of Physics, The Catholic University of America, Washington, DC 20064

[2]Observational Cosmology Laboratory, Code 665, Goddard Space Flight Center, Greenbelt, MD 20771

[3]Department of Physics and Astronomy, University of California Los Angeles, Los Angeles, CA 90095; current location, email: spetty@astro.ucla.edu

[4]Space Telescope Science Institute, 3700 San Martin Dr., Baltimore, MD 21218

[5]ESA Space Telescope Operations Division, MD 21218

One method of combining the light at multiple wavelengths to determine the integrated stellar properties of galaxies includes the fitting of photometric data with the overall shape of galaxy spectra, or spectral energy distribution (SED). The technique is well-established and first proposed by Baum (1962) for obtaining photometric redshifts of cluster galaxies. Since the mid-90's photometry became trusted as a reliable method for determining redshifts (e.g. Mobasher et al. 1996; Lanzetta, Fernández-Soto, & Yahil 1998; Hogg et al. 1998). It has proven to be invaluable, especially for deep and large surveys such as the HDF North and South, since spectroscopy is time consuming and not feasible for large galaxy surveys. Photometric redshifts are derived from strong spectral features, such as the Lyman-break (912 Å), the 4000 Å break, or the Balmer-break (3646 Å).

One main difficulty with observations of high redshift galaxies is correlating the observed properties with the appropriate rest-frame. Infrared (IR) observations of galaxies show the rest-frame near-IR (NIR) and optical for $z > 1$, while optical observations show the rest-frame ultraviolet (UV). At high redshifts, observing the rest-frame IR to identify thermal emission from star-forming regions becomes problematic in the FIR, because of the lower resolution images. Although optical observations provide better resolution images, dust significantly masks the light at rest-frame wavelengths blue-ward of ~ 3000 Å. This significantly limits the types of galaxies resolved at high redshift where photometry may be analyzed.

SEDs are determined from templates of local galaxies and this presents a problem when attempting to fit models for higher redshift objects. Despite these complications, many important discoveries have been made concerning the nature of high redshift galaxies using SEDs. One of the most observed are Lyman-break galaxies (LBGs), which are compact, starbursts that are rest-frame UV selected (see Steidel et al. 1996) for the presence of a prominent Lyman-break at 912 Å. The break is created by O and B stars that ionize hydrogen from the ground state. They have been identified from $z \sim 1$ to $z > 5$ (e.g., Steidel et al. 1996; Bouwens et al. 2006; Burgarella et al. 2007). Older stellar population galaxies, such as Balmer-break galaxies (BBGs) have a drop in flux at the Balmer 3646 Å, line. The Balmer-break marks the termination of the hydrogen Balmer series and is strongest in A-type stars, making it sensitive to stellar age.

In the optical rest-frame, the Balmer-break is often used to select for galaxies with more evolved stellar populations (e.g. Baum 1962; Franx et al. 2003; Mobasher et al. 2004; Wiklind et al. 2008). Franx et al. calculate a median age of 0.7-1 Gyr from a sample of $J_s - K_s$ selected galaxies at photometric redshifts ~ 3. A later paper by Wiklind et al. (2008) identifies galaxies at $z > 5$ using the 3.6 μm and K bands to detect the Balmer-break. They select 11 candidates with ages 0.2-1 Gyr, which implies extremely efficient star-formation processes in the early universe. Studies such as these provide evidence of evolved galaxies at high redshift, which is an important aspect to fully understanding galaxy evolution.

This paper includes the use of optical to MIR observations based on sources extracted from the Hubble Ultra Deep Field Follow-up Near Infrared Camera and Multi-Object Spectrometer (HUDF-NICMOS) parallel observations (UDF05; Stiavelli 2005), which is an extension of the NICMOS UDF Treasury Program (Thompson et al. 2005). Thompson et al. presented parallel observations of the HUDF with one subsection of the HUDF covered. Oesch et al. (2007, 2009) present results from this survey, showing observations of $z \gtrsim 5$ galaxies. These results are based on ACS observations on the Thompson et al. (2005) NICMOS parallel fields. The results in this paper are galaxies with redshifts $z \sim 1.5 - 4$, using the NICMOS observations, which are parallel to the ACS observations in the Stiavelli (2005) UDF05 study.

We describe the data reduction, source extraction, error analysis and catalog selection in §2. In §3, the SED fitting method is explained in detail. In §4, We provide results for a selection of the data, which includes Monte Carlo simulations to test the robustness of the SED results. We have adopted the cosmological constants $H_0 = 70\,\mathrm{km\,s^{-1}\,Mpc^{-1}}, \Omega_m = 0.3$, and $\Omega_\Lambda = 0.7$ throughout this research.

2. The Sample

The sample includes the multi-wavelength analysis of galaxies observed in the NICMOS parallel pointings in the Hubble Ultra Deep Field

Follow-up (UDF05; Stiavelli 2005). The UDF05 project is an HST Large Program of ultra-deep ACS/WFC and NICMOS observations. As shown in Figure 1, the ACS/WFC observed the original HUDF parallel fields NICP12 and NICP34, imaged by the NICMOS F110W (J_{110}) and F160W (H_{160}) filters and are not used in this paper. The UDF05 also conducted parallel NICMOS observations, where one of the pointings is on the original HUDF field (numbered regions in Figure 1). These parallel observations are the main source of photometry for our dataset. In addition to the multi-wavelength coverage, the reason for selecting the NICMOS parallel fields was to have coverage of multiple areas to reduce cosmic variance effects (Somerville et al. 2004).

This section discusses the data reduction, source extraction, catalog construction, and data selection techniques that we used for these data.

2.1. Data Reduction

We extract sources from five parallel fields, including the HUDF, for the main catalog. Figure 1 displays the fields for the HUDF and the HUDF parallels NICP12 and NICP34, along with the parallel NICMOS fields for the UDF05. Red boxes mark the 5 parallel UDF05 NICMOS fields. Each one has a reference number; for example, the HUDF pointing is Region 1. The total area covered by the 5 regions is ~ 5.7 arcmin^2.

The NICMOS images in the F110W (J_{110}) and F160W (H_{160}) filters were downloaded from the Multimision Archive at STScI (MAST) archival search tool. We followed the technique in Thompson et al. (2005) for the reduction of the images. The NIC3 camera has a pixel size of $0.2''$pix^{-1}, which makes it impossible to resolve some of the more compact galaxies at higher redshifts. To increase the sampling for each pixel, we drizzled the multiple pointings in each field together using the IRAF[1] tool MultiDrizzle to $0.09''$pix^{-1}. In the drizzling process, the MultiDrizzle parameter PIXFRAC was set to 0.6 and SCALE to 0.09/0.202863, which produced the $0.09''$pix^{-1}. The number of combined images for each field, the calculated exposure times, and the drizzled image sizes are listed in Table 1. The final processed images are displayed in Figure 2. They are ordered by region number from top to bottom, and the left and right columns are the J_{110}- and H_{160}-bands.

This project consists of multi-wavelength analysis, which includes observations in the optical (Advanced Camera for Surveys with the Wide Field Camera, ACS/WFC) and MIR (Spitzer Space Telescope with the Infrared Array Camera, SST/IRAC). For the optical wavelengths, we downloaded all data from MAST and used it as processed in the pipeline. For Region 1, the HUDF (Beckwith et al. 2006) ACS F606W (V_{606}), F775W (i_{775}), and F850LP (z_{850}) images were acquired from the MAST archive.

The other fields, Regions 2-5, are outside of the UDF and Great Observatory Origins Deep Survey (GOODS; Giavalisco et al. 2004) footprint, so only the ACS F606W (V_{606}) and F850LP (z_{850}) from the Galaxy Evolution From Morphology (GEMS; Rix et al. 2004) survey were available. The GEMS footprint only partially covered Region 5. GEMS has a $5\,\sigma$ depth of $m_{\rm AB}(V_{606}) = 28.3$ and $m_{\rm AB}(z_{850}) = 27.1$.

The ACS images ($0.05''$pix^{-1}) were rebinned to the drizzled NICMOS pixel size ($0.09''$pix^{-1}). They were then convolved with a NICMOS point-spread function (PSF) generated with the Tiny Tim (Krist 1993) modelling software. While this increases the error for the ACS photometry, it allows for better SED fitting since the magnitudes are measured over similar isophotal areas.

The Spitzer/IRAC filters include four channels (3.6, 4.5, 5.8, and 8.0 μm). All data were downloaded from the SST archive retrieval tool Leopard Version 9[2]. We obtained the Region 1 data from the GOODS Spitzer Legacy Science Program (Dickinson et al. 2004). The GOODS program reach $5\,\sigma$ depth at $m_{\rm AB} = 26.1$, 25.7, 23.8 and 23.7 for the 3.6, 4.5, 5.8, and 8.0 μm filters, respectively. We retrieved the images for Regions 2-5 from the Extended CDF-S program by van Dokkum et al. (2005) (SIMPLE program). For all IRAC data, we analyzed the Post-BCD mosaic images that have pixel scales of $0.6''$ with no further processing.

[1]Image Reduction and Analysis Facility is available at http://iraf.noao.edu/

[2]Leopard is available at http://ssc.spitzer.caltech.edu/propkit/spot/

2.2. Source Extraction

We used SExtractor (SE Bertin & Arnouts 1996) in dual-image mode for object detection. The primary image for NICMOS was the H_{160} filter. Table 2 lists the parameters used in the SE input file. For ACS source extraction, the z_{850} image was the primary image. The GOODS SE detection parameters were used with a few adjustments for background. For IRAC source extraction, the 3.6 μm image was used as the primary image and SE parameters came from Dickinson et al. (2004).

For the NICMOS drizzled images, the edges have a much smaller integration time compared to the inner portions of the image. In order to minimize this, we created masks for the outer edges in each image. The drizzled weight maps do account for some of this effect (the exposure time largely determines the weight image values), but further masking was needed to reduce the problems associated with edge-detections.

The photometric measurements are isophotal magnitudes for all ACS and NICMOS magnitudes, and 3″ diameter apertures are used for IRAC sources. The IRAC detections are known for problems with confusion due to its low resolution (i.e., overlap between sources that are too close to be resolved), so special care was introduced to handle this. We used a cross-catalog matching algorithm to indentify NICMOS objects that were multiple matches to IRAC detections and checked each multiple-match manually for blended sources. If a blended source was present, we masked (from SE segmentation maps), where possible, the obstructing object and re-measured the magnitude. If it was not possible to separate the sources, we removed them from the catalog. This affected only a handful of objects.

2.2.1. Photometric Errors

For the NICMOS objects, the errors include those calculated from Poisson noise in the weight maps and systematic errors. The systematic errors were determined by simulating galaxies at random positions and comparing the SE measured magnitudes with the input magnitudes (see §2.4). The error is then calculated by $\Delta m = (m_{\rm in} - m_{\rm out})$, where $m_{\rm in}$ is the input (model) magnitude and $m_{\rm out}$ is the SE measured magnitude. This is the same method applied by Giavalisco et al. (2004). The standard deviation of the Δm distribution is $\sim 0.05\, m_{\rm AB}$, which is added in quadrature to the SE measured errors. We also added (in quadrature) 0.07 $m_{\rm AB}$ for NICMOS as a lower limit for the error, based on the ACS systematic errors determined by Giavalisco et al. (2004). The reason is that NICMOS, which is much lower signal-to-noise and has less resolution, will introduce more error into the photometry. Therefore, the NICMOS measurements will have, as a lower limit, the ACS systematic error (T. Dahlen 2009, private communication).

2.3. Catalog Construction

To create the final catalog, all SE catalogs were matched by RA and DEC. The catalog is based on the NICMOS H_{160}-band detections. The multi-wavelength catalogs created from SE were cross-matched using an automated program, which included flags for multiple matches and cases with no matches. The multiple matched objects were checked manually and the catalog was adjusted accordingly. For example, in the case of confusion the competing objects were masked and the object of interest measured again. Also, objects deblended in the ACS, may not have been deblended in NICMOS because the point spread functions are dissimilar in different bandpasses. In these cases, we re-measured the NICMOS magnitudes, so that SE would not deblend these.

Any object missing in the J_{110}-band was removed, which proved to be a useful check, since many of the non-detections in the J_{110}-band were very faint and beyond the detection limits in the H_{160}-band image ($m_{\rm AB} \gtrsim 26$ see §2.4). This resulted in a total of 630 objects.

The NICMOS photometry was checked against Thompson et al. (2005) and we found an offset of ~ 2.3 for the H_{160}-band and ~ 1.5 for the J_{110}-band, where our data are brighter by this amount. This difference is probably due to: 1) background subtraction in the drizzling process; 2) different methods of estimating the background in source extraction. We added the offsets to calibrate the data with the Thompson et al. magnitudes. A check was also conducted by fitting SEDs to a few objects, which determined that the objects with the calibrated magnitudes resulted in more robust fitting.

2.4. Detection Completeness

To calculate the completeness, we used the NIC3 H_{160}-band filter images and inserted artificially created galaxies into each region. We extracted sources with SE based on the method above. We randomly generated 500 galaxies of de Vaucouleurs (disk galaxies with surface brightness distributions $\propto (r/r_e)^{1/4}$) and elliptical profiles at varying luminosities and at random positions, using the IRAF tool artdata. These were added to the H_{160}-band images. A polynomial was fit to the detection ratio and magnitude values. We recover 80% of the artificially generated sample at $m_{\rm AB} = 25.4$ and 50% at $m_{\rm AB} = 26.7$. Figure 3 is a plot of the detection ratio with $m_{\rm AB}$ for the H_{160}-band images. We calculated the completeness values at the 50% and 80% detection ratios by solving a polynomial fit (dashed line) at those points.

Figure 4 displays the $m_{\rm AB}$ distribution for the V_{606}, z_{850}, J_{110}, and H_{160} filters of the actual detections (not artificially generated objects). The $m_{\rm AB}$ are noticeably higher for the optical, especially the V_{606}-band, which is to be expected. One reason for this is that the signal-to-noise (S/N) is much higher for observations in the optical compared to the NIR. Also, depending on the rest-frame wavelength, a dusty or older population galaxy will register a higher flux for wavelengths red-ward of rest-frame wavelengths. For example, Figure 5 (discussed in §3) shows much brighter NIR rest-frame flux for the older 290 Myr and 1.4 Gyr galaxies. For higher redshift galaxies ($z \gtrsim 1$), this results in a larger magnitude in the V_{606}-band compared to the J_{110}- and H_{160}-bands for the same object.

3. Spectral Energy Distributions

The SED modelling in this paper is based on Bruzual & Charlot (2003) (hereafter BC03) with Charlot & Bruzual (2007) (hereafter CB07) adaptations for handling the TP-AGB phase (thermally pulsating asymptotic giant branch stars).

In our data, the location of the Balmer-break ($\lambda_{RF} = 3646$ Å) with respect to the observed wavelength is important, since the SED fitting method used for our photometry exploits this feature to identify the best-fit SED. The Balmer-break is most prominent in A stars, since in O and B stars the hydrogen is mostly ionized, and is a useful age diagnostic for galaxies between 0.1 to 1.0 Gyr.

3.1. SED Parameters

The parameters obtained from SED fitting rely upon proper redshift fitting. The method applied in this paper is a standard χ^2 minimization technique. Generally, the SED fitting is employed with a set of a priori conditions on the parameters determined by the spectra (metallicity, dust extinction, starburst age, etc.). For this dataset, the observed photometric points from the catalog are compared to a set of template spectra generated from the BC03/CB07 libraries and with a large parameter space for redshift, starburst age ($t_{\rm sb}$), extinction (E_{B-V}), metallicity (Z) and star formation e-folding decay time (τ). While the parameter space allows for an unbiased and prior-free SED fitting, there are cutoffs which apply hidden priors. Also, the number of filters used for photometry is very important in determining the χ^2 value, since the number of photometric data points limits the number of parameters that define the SED.

The SED colors are evaluated in fixed observed bands (HST ACS: V_{606}, i_{775}, and z_{850}; HST NICMOS: J_{110} and H_{160}; Spitzer IRAC: 3.6, 4.5, 5.8, and 8.0 μm). The ranges and cutoffs for the parameters are similar to Wiklind et al. (2008): $z = 0.1 - 9$ with $\Delta z = 0.1$, $E_{B-V} = 0.0 - 0.95$ with $\Delta E_{B-V} = 0.025$, $\tau = 0.0 - 1.0$ Gyr with $\Delta\tau = 0.1$, and Z = 0.2, 0.4, 1.0, and 2.5 $Z_\odot$. The starburst age ranges from $t_{\rm sb} = 0.005 - 2.4$ Gyr with steps of 5 Myr for $t_{\rm sb} \leq 0.1$ Gyr and age steps of 100 Myr for $t_{\rm sb} > 0.1$. For comparison with the age of the Universe, at $z \sim 2.7$ the Universe was approximately 2.4 Gyr.

To account for inter-galactic medium (IGM) attenuation due to neutral hydrogen absorption, the Madau (1995) prescription is used for the mean IGM opacity. Madau provides transmission curves for high-z ($2.5 < z < 4.0$) galaxies as a function of observed wavelength, which can be used to correct the flux based on the redshift or rest-frame wavelength. The magnitudes can increase by ~ 2 in the redshift range $2.5 < z < 4.0$. The dust extinction E_{B-V} was calculated using the attenuation law from Calzetti et al. (2000) and is parameterized through the E_{B-V} color index. The bolometric luminosity ($L_{\rm Bol}$) is derived

by integrating over the entire wavelength range (91 Å to 160 μm). The SED output provides L_{Bol} with and without dust corrections, which gives a method for estimating the FIR luminosity (L_{FIR}). Calzetti et al. (2000) define the color excess based on comparisons between the UV and FIR flux for starburst galaxies. They determine that $\sim$ 30% of the bolometric flux is from the UV-NIR wavelength range and the rest is emitted in the FIR. By assuming that dust absorption of the UV-optical is re-emitted in the FIR, the FIR luminosity can be approximated by calculating the excess. All SED values for FIR luminosity in this paper are given by $L_{FIR} = L_{Bol} - L_{Bol_E}$, where L_{Bol_E} is the bolometric luminosity corrected for dust.

The SSPs in BC03 give the stellar mass-to-light ratio M^*/L_V based on the V-K and B-V colors and metallicity. As reddening and metallicity increases, so does the M^*/L_V. The physical reason for this is that, for a fixed stellar mass, lowering the metallicity causes stars to evolve at higher effective temperatures and luminosities (Schaller et al. 1992; Fagotto et al. 1994; Girardi et al. 2000). After identifying the best-fit model, the stellar mass M^* is calculated by simply multiplying L_{Bol} by M^*/L_V. The star formation rate (SFR) is calculated through an exponential declining function, based on the e-folding time (τ) and the starburst age (t_{sb}) and results are discussed in §4.2.

Several million models are pre-calculated, spanning the predefined parameter spaces. The resulting SEDs are integrated through filter response functions for the appropriate filter, which are then best-fit with the observed photometry using χ^2 minimization.

4. Results

We created a subsample of 301 objects out of 630 in the main catalog. This selection is based on the number of free parameters used for fitting the SEDs (described in §3). Since there are five parameters, at least five photometric values must be present for a proper fit, which resulted in 301 objects. Most of these objects had no IRAC detections, which makes the sample limited to the IRAC sensitivities. Because the sources are selected from the H_{160}-band, the sample is more sensitive to stellar mass than UV luminosities.

4.1. Validity of Photometric Redshifts

Figure 6 displays the distribution of photometric redshifts, or z_{phot} , obtained from the SED fitting. There are noticeable peaks that indicate both the strengths and weaknesses of the Balmer-break technique. Because the Balmer-break occurs at 3646 Å, for any galaxy at $z < 0.5$ ($\lambda_{RF} \lesssim$ 6000 Å) the break will not be detected in this sample. This is a selection effect from the limited optical photometric bands; the ACS-V_{606} covers the edge of this break at this redshift limit. Without the ACS-B_{435}-band the break cannot be determined at lower redshifts (see Figure 5). A strength for the technique with this sample occurs for $z > 1.3$ ($\lambda_{rest} \gtrsim$ 9200 Å), where the ACS-z_{850} and NICMOS coverage is applicable for $1.3 \lesssim z \lesssim 3.5$. At even higher redshifts, the IRAC images provide the signatures of the Balmer-break, but significant problems may arise from the large errors and confusion intrinsic with infrared imaging, due to the low resolution of Spitzer.

In order to determine the efficacy of the z_{phot} results, we matched multiple spectroscopic redshift catalogs with the main SED catalog and found 16 objects (Objects 7, 13, 15, 21, 24, 25, 38, 58, 71, 76, 78, 102, 119, 133, 144, and 204). Figure 7 shows the comparison between the z_{phot} and spectroscopic redshifts (z_{spec}) for these 16 objects. They are discussed in more detail in the following section. Figure 7 compares z_{spec} and z_{phot} using $\Delta = (z_{phot} - z_{spec})/(1 + z_{spec})$. This is a standard method to determine the fractional error (see Mobasher et al. 2004). The figure lists the median error, $< \Delta >$, the rms scatter σ. The small number of objects biases our results, but there is a clear separation between z_{phot} obtained for $z < 1$ and $z > 1$. The objects at higher redshifts ($z \gtrsim 1$) have z_{phot} that agree well with the spectroscopically confirmed redshifts. Out of the 16 galaxies, 75% have Δ within ± 0.2.

4.2. Objects with Spectroscopic Redshifts

Figures 8-9 show eight greyscale images for the 16 objects that have available spectroscopic redshifts. The images in the top row are: ACS V_{606}, z_{850}, and NICMOS J_{110}, H_{160}. The IRAC images are in the bottom row for Ch1 , Ch2, Ch3, and Ch4 (3.6, 4.5, 5.8, and 8.0 μm) as labeled. A 1″ ruler marker is provided for each image.

The best-fit SEDs are shown in the Figure 10. The SED shows the observed and rest-frame wavelengths marked as the bottom and top abscissa, respectively. The magnitudes are listed in AB, which is the same as the photometric data in the main catalog. The two different SED lines refer to the flux corrected for dust and flux without dust corrections (red and blue, respectively in online color figure). Plots with only one line have E_{B-V} = 0, so no dust corrections are calculated. This is the case for objects 38, 58, 76, 144, and 204.

Table 3 gives a list of the 16 objects with spectroscopic redshifts and their best-fit parameters. Of special note are the 11/16 galaxies with $\Delta \lesssim 0.2$, which are specified with an asterisk. Galaxies with the highest redshifts are Objects 24 and 38 at $z_{\rm spec} = 3.6$ and 5.95.

In Figure 8, Object 24 has a very bright lenticular structure with a young ($t_{\rm sb}$ = 10Myr) dusty-starburst SED template. It appears as an edge-on disk in the ACS V_{606} and z_{850}, and has a prominent bulge in the NICMOS images. The ACS corresponds with the UV rest-frame, while the NICMOS corresponds with the optical rest-frame. This object has an effective radius of 0.54″ in the observed NIR, or $\sim$ 4.5 kpc at z = 3.6. It is extremely massive, with a stellar mass of $\sim 10^{12}\,M_\odot$. Based on the SED-derived $L_{\rm FIR}$, this is a ULIRG at $z \sim 4$. A Spitzer MIPS detection is inconclusive, because the pixel scale is 2.45″pix^{-1}; one pixel is twice the size of the object. It is the most massive and FIR-luminous out of the 11 spectroscopic redshift objects.

Object 38 is not well resolved, but appears to be a clumpy, compact galaxy. In Figure 8 the detection is very faint in the optical-NIR and "drops out" in the V_{606}-band. It also has SED features of a young ($t_{\rm sb}$ = 10Myr) starburst, but with no dust correction. The effective radius is 0.27″ in the observed NIR, which is equal to $\sim$ 1.5 kpc at z = 5.9. It has a stellar mass of $\sim 10^8\,M_\odot$ and $L_{\rm FIR} \sim 10^{10} L_\odot$. This is a compact dust-free starburst galaxy and fits all the properties of being an LBG at $z \sim 6$.

Objects 76, 102, 119 and 133 have $z_{\rm spec} \sim 1.3$. All but one (Object 76) have IRAC photometry. In Figure 9, Object 76 shows itself as a very thin, wispy feature in the V_{606} and z_{850} (rest-frame FUV and U-band). In the NICMOS images, the galaxy pops out to almost a magnitude brighter (rest-frame optical). The effective radius is 0.62″ in the observed NIR, or $\sim$ 5.23 kpc at z = 1.3. The SED displays a dust-free older star-forming galaxy ($t_{\rm sb}$ = 100 Myr), where the Balmer-break is stronger from the O and B stars moving out of the main sequence. It has a stellar mass of $\sim 10^8\,M_\odot$ and $L_{\rm FIR} \sim 10^9\,L_\odot$.

Object 102 (Figure 9) also has a thin appearance in the ACS, or rest-frame UV, images. In the NICMOS, or rest-frame optical, an outer disk of older population stars appears. The effective radius is 0.42″ in the observed NIR, or $\sim$ 3.5 kpc at z = 1.3. The SED is modeled by a very dusty (E_{B-V} = 0.375), highly star-forming (SFR$_{ave} \sim 49 M_\odot {\rm yr}^{-1}$) plus an older starburst age ($t_{\rm sb}$ = 100Myr). The Balmer-break is a tiny decrement in the z_{850}-J_{110} observations. It has a stellar mass of $\sim 10^9\,M_\odot$ and $L_{\rm FIR} \sim 10^{11} L_\odot$.

In Figure 9, Object 119 appears bright in the rest-frame UV as an irregularly shaped, inner core in the ACS filters. Its reddened outer shell appears bright in the NICMOS images. There is confusion in IRAC with a bright feature in the lower left. This galaxy is compact with an effective radius of 0.23″ in the observed NIR, or $\sim$ 1.9 kpc at z = 1.3. The SED is fit to a young dusty starburst ($t_{\rm sb}$ = 30 Myr) and displays a bright MIR bump, which may be falsely augmented by confusion. The dust extinction (E_{B-V} = 0.375), $L_{\rm FIR}$ ($\sim 10^{11}\,L_\odot$) and M* ($\sim 10^{10}\,M_\odot$) are all similar to Object 102, which also has a slight MIR bump.

For objects 15, 25, 58, 71, and 78 the SED fits are remarkably close and redshifts are at $z \sim 1$ (see Figure 10). Object 15 is clumpy and disturbed morphologically. It appears to have been in a recent merger in the ACS images, where very patchy clumps of star-forming regions are seen in the rest-frame NUV (observed V_{606}). The galaxy becomes a bulge-dominated elliptical in the rest-frame optical (observed H_{160}). Object 71 also has a clumpy rest-frame NUV morphology and becomes an extremely bright rest-frame optical through MIR source (observe z_{850}-IRAC 4). The Balmer-break has blended with the 4000 Å break, which fits an older 1.02 Gyr galaxy with little dust extinction. The remaining objects have very similar morphologies at different wavelengths.

All objects with insufficient fits for $z_{\rm phot}$ values occur for $z_{\rm spec} \lesssim 1.3$, which as discussed above in §3 is a weak region for the Balmer-break to be

detected with this photometric dataset. Additionally, many of the IRAC detections have confusion or are non-existent, which causes a crude fit. Object 7 is an example, where no IRAC detection is present and $z_{\rm phot} = 4.3$ for a $z_{\rm spec} = 1.03$ object. It should also be noted that objects 7-133 with spectroscopic redshifts are in Region 1, which is part of the HUDF. We obtained i_{775}-band photometry for this pointing, which extended the SED coverage between the V_{606}- and z_{850}-bands.

Three objects (21, 24 and 78) have unrealistic star formation rates (see Table 3). They are fit with SEDs that have dusty, instantaneous bursts ($\tau = 0$) with starburst ages 10 Myr. This is tested in the Monte Carlo simulations in the following section. By fixing $z_{\rm phot}$, thereby reducing the number of free parameters, a more likely age and star formation rate is generated. Even though $z_{\rm phot}$ is correct for object 24, the age and star formation rate is unlikely to be real. The results for $z_{\rm phot}$ and mass are more robust than the age and star formation rate, due to SED fitting methods. Lee et al. (2009) determine that the stellar mass is underestimated by 19%-25%, because of older stellar populations being hidden by recent star formation. Furthemore, they find the star formation rate is less robust due to various star formation histories in galaxy templates, and the degeneracy between age and dust extinction.

4.3. Monte Carlo Simulations

The foremost potential source of systematic errors in SED fitting is the reliability of the photometric redshifts, which we tested, as mentioned above, by comparing with the available spectroscopic redshifts. Indirect testing may also be performed for all the objects through Monte Carlo simulations. These simulations also check for the reliability of other parameters that are also vulnerable to erroneous values. The Monte Carlo simulations provide the probability distribution of the parameters. The simulations consist of pseudo-random re-sampled magnitudes, within the given photometric errors. Slight shifts in the magnitudes can create different stellar population models to be fit to the input SEDs, but should give a normal distribution around a peak for a robust fit.

Table 4 shows the parameter values for the Monte Carlo simulations for all objects with spectroscopically confirmed redshifts. For each object, there are two sets of parameters. The first set allows for the redshift to be a free parameter in the fitting (top). The second set gives results for a constant redshift at $z_{\rm spec}$ (bottom). These results include 500 simulations for each object, giving the probability density of a certain value. All values presented are the distribution peak value unless indicated otherwise. Columns 2 and 3 list the redshifts for the Monte Carlo distribution peak ($z_{\rm mc}$) and the best-fit ($z_{\rm phot}$). Column 4 gives the percentage of the simulated fits that obtained the $z_{\rm phot}$ value. Columns 5-10 are: the E_{B-V}, the metallicity, $L_{\rm Bol}$ without dust correction, M*, mean $\rm SFR_{ave}$, mean $t_{\rm sb}$. Note that the $z_{\rm phot}$ obtained from the SED fitting does not necessarily agree with the most likely median value in the Monte Carlo simulations. This is probably caused by the relatively flat SED and the number of degrees of freedom in the SED fitting process compared to the number of photometric points. Setting the redshift to a constant shows more realistic values in terms of the star formation rates, indicating that the number of photometric points is a cause of the multiple peaks in the Monte Carlo simulations.

4.3.1. Three Study Cases

The parameter distributions in Figure 11 often show multiple peaks. The presence of the multiple peaks indicates that there is a certain probability for the SED to fit that value. We discuss the results for three galaxies based on the several possible parameters that could

Object 24 (top panel in Figure 11) is an example of an object where the Monte Carlo distribution peak redshift, $z_{\rm mc}$, agrees well with both $z_{\rm phot}$ and $z_{\rm spec}$. The redshift is narrowly distributed, while the double peaks for other parameters indicate a significant likelihood for the two values. The stellar mass, dust extinction, and luminosity result in best-fit values within the distribution of these peaks and are not too different from the maximum from the Monte Carlo distribution.

Object 25 (middle panel in Figure 11) is one of the typical results, where $z_{\rm mc}$ (3.8) does not agree well with $z_{\rm phot}$ (1.1) and $z_{\rm spec}$ (1.09). All the parameters have multiple peaks, where the best-fit result is located within one of the peak distributions (not necessarily the most populated).

Object 144 (bottom panel in Figure 11) is an example of one of the worst fits, where $z_{\rm mc}$ (5.7), $z_{\rm phot}$ (0.1) and $z_{\rm spec}$ (0.54) do not agree and the parameters have very noisy distributions. The 8.0 μm IRAC magnitude has a very large error and this is very likely what contributes to the complicated distribution for redshift, which then makes the remaining parameters difficult to fit.

As a representative sample, the spectroscopically confirmed objects have 4 good fits similar to Object 24, 8 typical fits similar to Object 25 and 4 bad fits similar to Object 144. Statistically this means that the SED fitting method works for approximately 75% of the objects at $z \gtrsim 1.3$. A larger number of objects with spectroscopically confirmed redshifts is needed to validate this trend. However, the Monte Carlo method is a powerful tool in evaluating the SED fits and provides confidence when evaluating the results of the fit.

4.4. Galaxies at $z\sim$1.3 and 4

We selected galaxies, from the SED output catalog, that are in the redshift ranges $1.3 \leq z \leq 2$ (35 objects) and $3 \leq z \leq 4$ (31 objects) and that also had at least one IRAC detection. The purpose of the redshift selection is that these redshifts have been shown (see §4.1) to be appropriate for Balmer-break detection with our photometric data. The IRAC photometry helps constrain the fit for the rest-frame NIR to MIR stellar population and tend to have better agreement with $z_{\rm spec}$. Six of these objects (Objects 38, 58, 76, 102, 119, and 133) have $z_{\rm spec}$ and agree with the trends described below.

Figure 12 shows six histograms with distributions of SED parameters. The diagonally hatched bars depict galaxies with spectroscopic redshifts at $1.3 \leq z \leq 2$ (objects 76, 102, 119, 133) and $z > 3$ (objects 24 and 38), respectively. Several noticeable trends are immediately apparent. In the top right plot, it is clear that the higher redshift galaxies have less dust extinction. This is a selection effect, because the rest-frame UV is observed by optical wavelengths for the higher redshift population. The UV light is highly absorbed by dust. Any object too faint from dust extinction, and not detected in the UV rest-frame would not have the required photometric points for SED fitting. One way to solve this is by having more IR photometry and JWST will provide the photometry necessary to extend the SED at these redshifts.

The luminosities and star formation rates show brighter sources for higher redshifts. The increase in luminosity at $z \sim 3-4$ agrees with Bouwens et al. (2007), which show a peak SFR density at this redshift range. Although, one might argue that this is Malmquist bias, it has been shown that the luminosity increase for $z \sim 2-6$ galaxies is not a selection effect (Bouwens et al. 2004, 2007). These authors used the sizes and magnitudes of galaxies in the UDF and GOODS and found that the GOODS objects represented the same sample, even though it is not as deep of a survey as the UDF.

The stellar mass appears to be hovering around the same median point for both redshift ranges. In general, the majority of bolometric luminosity originates from massive stars. From where is the higher luminosity originating at higher redshifts? This is most likely caused by the limits in the Salpeter IMF used in the SED code. In general, the majority of light measured from galaxies is produced from a few massive stars, while the less massive stars contribute most of the stellar mass. Furthermore, previous analyses have shown that there is a shortfall in ionizing photons to produce Ly-α flux at the re-ionization epoch ($z \sim 7$) using current stellar population models (e.g., Bromm, Kudritzki, & Loeb 2001; Schaerer 2003; Bunker et al. 2009). One solution proposed includes increasing the IMF mass limit to a top-heavy IMF or to decrease metallicities. However, Franx et al. (2008) show that the stellar mass density increases with redshift for a given mass. Also, it may be due to evolution of the fundamental plane, where the mass-to-light ratio decreases with redshift and can be modelled by the evolution of a simple stellar population (see van Dokkum & van der Marel 2007, and references therein).

5. Summary

We extracted sources observed in the parallel NICMOS UDF05 fields and selected galaxies to calculate SEDs. A total of 630 galaxies were cross-matched using the ACS filters V_{606} and z_{850}, NICMOS filters J_{110} and H_{160}, and Spitzer IRAC channels 1-4. The photometry are sensitive to stellar mass, because the sources are H_{160}-band

selected A selection of 301 objects were modeled with spectral energy distributions using χ^2 minimization. Photometric redshifts, dust extinction, stellar masses, bolometric luminosity, starburst age and metallicity were estimated to analyze galaxy evolution over a select range of redshifts.

The main results are:

1. The redshift distribution for 301 photometric redshifts shows a patchy, non-normal distribution. This is a result of the wavelength coverage, where the data is not sensitive to strong spectral features, such as the Balmer-break, which is sensitive to stellar age. It was shown with simple stellar population models that the break might be detected at $z \gtrsim 1.3$ with the given photometry.

2. Comparisons with 16 spectroscopic redshifts give 75% within $\Delta \leq 0.2$. These photometric redshifts are in accord with the sensitivities expected from the Balmer-break with this dataset. The accuracy of the photometric redshifts may be improved with color selection criteria.

3. A case study of the Monte Carlo simulations determines that the parameters from the best-fit SEDs are robust for the redshift ranges $z \gtrsim 1.3$.

4. We analyze a subsample of galaxies at photometric redshifts 1.3-2 (35 objects) and 3-4 (31 objects) and determine that L_{Bol} and SFR increase significantly from $z \sim 1.5$ to 4. This agrees with previous results by Bouwens et al. (2007), and is not a selection effect. Dust extinction decreases, but this is due to a selection effect, where the rest-frame UV and optical are observed in the optical and NIR at $z \sim 4$. The dust will absorb these wavelengths, which limits the photometric detections.

5. Objects 24 and 38 are the highest redshifts that are spectroscopically confirmed at $z \sim 3.7$ and 6. The SED model for Object 24 gives $L_{FIR} = 10^{13}$ $L_{\odot}$, which would make it a ULIRG at $z = 3.7$.

6. Objects 76, 102, 119, and 133 are objects with spectroscopically confirmed redshifts at $z \sim 1.5$. Objects 102, 119, and 133 have starburst ages $t_{sb} \leq 50$ Myr, and are actively forming stars. Object 76 is probably an older 100 Myr starburst with little active star formation.

In future surveys, Objects 133, 24 and 38 are good candidates for JWST and ALMA. Object 133 is a galaxy that formed when the Universe was ~ 4.5 Gyr old. An instantaneous starburst with very high metallicity (2.5 $Z_o dot$) fits the SED, implying previous multiple starbursts. JWST would easily resolve the rest-frame MIR features which are not clear in IRAC, due to confusion and low resolution. Similarly, Object 24 is an example of a galaxy that formed when the Universe was ~ 1.6 Gyr old. It is possibly a ULIRG and is an example of a progenitor to nearby massive ellipticals. Object 38 is a more evolved galaxy (~ 1 Gyr) at $z \sim 5.8$ and is possibly among the first generation of galaxies. A follow-up study on these galaxies and similar types, with the JWST and ALMA observatories would provide better resolution in the NIR-millimeter wavelengths (optical-FIR rest-frames), which is important for distinguishing dusty star-forming galaxies, dust-obscured AGN and more evolved stellar populations. The new observatories will reveal the nature of these distant objects and how they connect with the local universe.

It is important to include high redshift observations of the more evolved stellar populations, because there has been a heavier emphasis on detecting LBGs and dusty starbursts at high redshifts, where more modest star-forming galaxies are not selected. This biases galaxy evolution models toward a younger population of galaxies. A comparison of the young, starburst galaxies with the more modestly star-forming galaxies can lead to an extensive view of galaxy evolution. The older stellar populations at high redshifts, after all, were the new stars of the first galaxies.

We are grateful to T. Dahlen for providing guidelines for NICMOS photometry. We also thank R.-R. Chary for correspondence concerning Spitzer/IRAC photometry, and for providing parameters for source extraction. S.M.P. was funded by NASA's NNX07AJ95G. D.F.dM. was funded by NASA's NNX07AR82G.

The HST data in this paper were obtained from

MAST at the Space Telescope Science Institute (STScI). STScI is operated by the Association of Universities for Research in Astronomy, Inc., under NASA contract NAS5-26555. Support for MAST for non-HST data is provided by the NASA Office of Space Science via grant NAG5-7584 and by other grants and contracts. This work is based [in part] on archival data with the Spitzer Space Telescope, which is operated by the Jet Propulsion Laboratory, California Institute of Technology under a contract with NASA. Support for this work was provided by NASA.

REFERENCES

Baum, W.A. 1962, in Proceedings from IAU Symposium no. 15, ed. G.C. McVittie, Macmillan Press (New York), 390

Beckwith, S.V.W., et al. 2006, AJ, 132, 1729

Bertin, E., & Arnouts, S. 1996, A&AS, 117, 393

Bouwens, R.J., Illingworth, G.D., Blakeslee, J.P, Broadhurst, T.J., & Franx, M. 2004, ApJ, 611, L1

Bouwens, R.J., Illingworth, G.D., Blakeslee, J.P., & Franx, M. 2006, ApJ, 653, 53

Bouwens, R.J., Illingworth, G.D., Franx, M., & Ford, H. 2007, ApJ, 670, 928

Bromm, V., Kudritzki, R.P., & Loeb, A. 2001, ApJ, 552, 464

Bruzual, G., & Charlot, S. 2003, MNRAS, 344, 1000

Bunker, A., et al. 2009,ArXiv Astrophysics e-prints, arXiv:0909.2255

Burgarella, D., Le Floc'h, E., Takeuchi, T.T., Huang, J.S., Buat, V., & Rieke, G.H. 2007, MNRAS, 380, 986

Calzetti, D., Armus, L., Bohlin, R.C., Koornneef, J., & Storchi-Bergmann, T. 2000, ApJ, 533, 682

Calzetti, D., et al. 2007, ApJ, 666, 870

Cardiel, N., et al. 2003, ApJ, 584, 76

Casertano, S., et al. 2000, AJ, 120, 2747

Chabrier, G. 2003, PASP, 115, 763

Chapman, S.C., et al. 2000, MNRAS, 319, 318

Chary, R., & Elbaz, D. 2001, ApJ, 556, 562

Charlot, S., & Bruzual, G. 2007, in preparation.

Dickinson, M., et al. 2004, "Great Observatories Origins Deep Survey (GOODS)", Spitzer Proposal ID #169

Fagotto, F., Bressan, A., Bertelli, G., & Chiosi, C. 1994, A&AS, 104, 365

Fioc, M., & Rocca-Volmerange, B. 1997, A&A, 326, 950

Franx, M., et al. 2003, ApJ, 587, L79

Franx, M., van Dokkum, P.G., Förster Schreiber, N.M., Wuyts, S., Labbé, I., & Toft, S. 2008, ApJ, 688

Giavalisco, M., et al. 2004, ApJ, 600, L93

Girardi, L., Bressan, A., Bertelli, G., & Chiosi, C. 2000, A&AS, 141, 371

Heckman, T.M., et al. 2005, ApJ, 619, L35

Hibbard, J.E. & Vacca, W.D. 1997, AJ, 114, 1741

Ho, L.C., & Keto, E. 2007, ApJ, 658, 314

Hogg, D.W., et al. 1998, AJ, 115, 1418

Holland, W.S., et al. 1999, MNRAS, 303, 659

Holwerda, B.W. 2005, ArXiv Astrophysics e-prints, arXiv:astro-ph/0512139

Hopkins, A.M., Connolly, A.J., Haarsma, D.B., & Cram, L.E. 2001, AJ, 122, 288

Kennicutt, R.C. 1998, ARA&A, 36, 189

Kennicutt, R.C., et al. 2009, ApJ, 703, 1672

Krist, J. 1993, Astronomical Data Analysis Software and Systems II, A.S.P. Conference Series vol. 52, R. J. Hanisch, R. J. V. Brissenden, and Jeannette Barnes, eds., 536

Kroupa, P. 2001, MNRAS, 322, 231

Labbé, I., et al. 2003, AJ, 125, 1107

Lanzetta, K.M., Yahil, A., & Fernández-Soto, A. 1996, Nature, 381, 759

Lanzetta, K.M., Fernández-Soto, A., & Yahil, A. 1998, in The Hubble Deep Field : Proceedings of the Space Telescope Science Institute Symposium, eds. M. Livio, S.M. Fall, & P. Madau, Cambridge Univ. Press (New York), 143

Lee, S.-K., Idzi, R., Ferguson, H.C., Somerville, R.S., Wiklind, T., & Giavalisco, M. 2009, ApJS, 184, 100

Le Févre, O., et al. 2004, A&A, 428, 1043

Leitherer, C., et al. 1999, ApJ, 123, 3

Lilly, S.J., Tresse, L., Hammer, F., Crampton, D., & Le Fevre, O. 1995, ApJ, 455, 108

Lotz, J.M., Madau, P., Giavalisco, M., Primack, J., & Ferguson, H.C. 2006, ApJ, 636, 592

Madau, P. 1995, ApJ, 441, 18

Madau, P., Ferguson, H.C., Dickinson, M.E., Giavalisco, M., Steidel, C.C., & Fruchter, A. 1996, MNRAS, 283, 1388

Magdis, G.E., Rigopoulou, D., Huang, J.-S., Fazio, G.G., Willner, S.P., & Ashby, M.L.N. 2008, MNRAS, 386, 11

Maraston, C. 2005, MNRAS, 362, 799

Meurer, G.R., Heckman, T.M., & Calzetti, D. 1999, ApJ, 521, 64

Meurer, G.R., et al. 2000, ArXiv Astrophysics e-prints, arXiv:astro-ph/0011201

Mobasher, B., Rowan-Robinson, M., Georgakakis, A., & Eaton, N. 1996, MNRAS, 1996, 282, L7

Mobasher, B, et al. 2004, ApJ, 600, L167

Oesch, P.A., et al. 2007, ApJ, 671, 1212

Oesch, P.A., et al. 2009, AJ, 690. 1350

Overzier, R., et al. 2008, ApJ, 677, 37

Overzier, R., et al. 2008, ApJ, 710, 979

Peacock, J. A., et al. 2000, MNRAS, 318, 535

Petty, S.M., et al. 2009, AJ, 138, 362

Polletta, M., et al. 2007, ApJ, 663, 81

Rieke, G.H., et al. 2009, ApJ, 692, 556

Rix, H.-W., et al. 2004, ApJS, 152, 163

Salpeter, E.E. 1955, ApJ, 479, 764

Scalo, J. 1998, in The Initial Stellar Mass Function, eds. Gilmore G. & Howell, D., Astron. Soc. Pac., San Francisco, ASP conf. Ser. Vol. 142, 201

Schaerer, D. 2003, A&A, 397, 527

Schaller, G., Schaerer, D., Meynet, G., & Maeder, A. 1992, A&AS, 96, 269

Somerville, R.S., Lee, K., Ferguson, H.C.. Gardner, J.P., Moustakas, L.A., & Giavalisco, M. 2004, ApJ, 600, L171

Stiavelli, M. 2005, "Searching for galaxies at $z > 6.5$ in the Hubble Ultra Deep Field", HST Proposal ID #10632

Steidel, C.C., Giavalisco, M., Pettini, M., Dickinson, M., & Adelberger, K.L. 1996, ApJ, 462, L17

Szokoly, G.P., et al. 2004, ApJS, 155, 271

Thompson, R., et al. 2004, AJ, 130, 1

Tinsley, B.M. 1980, Fundamentals of Cosmic Physics, 5, 287

Toft, S., et al. 2005, ApJ, 624, L9

van Dokkum, P., et al. 2005, "A Public Deep IRAC Survey in the Extended CDF-South", Spitzer Proposal ID #20708

van Dokkum, P.G., & van der Marel, R.P. 2007, ApJ, 655, 30

Vanzella, E., et al. 2006, A&A, 454, 423

Weedman, D.W., & Huenemoerder, D.P. 1985, ApJ, 291,72

Wiklind, T., et al. 2008, ApJ, 676, 781

Wuyts, S., et al. 2007, AJ, 655, 51

This 2-column preprint was prepared with the AAS LaTeX macros v5.2.

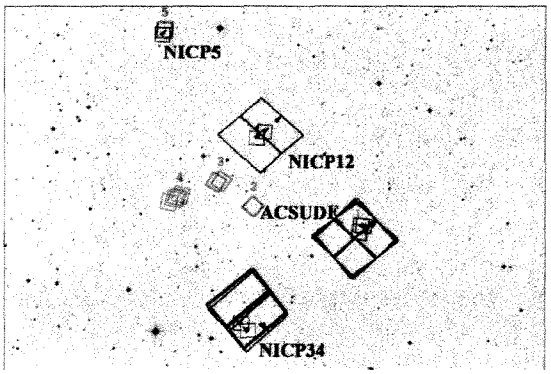

1.)

Fig. 1.— Footprints of the UDF05 NICMOS parallel fields. The image displays the original HUDF field with the parallel fields NICP12, NICP34, and NICP5 overlayed on a DSS image (Stiavelli 2005). The small boxes, numbered 1-5, indicate the UDF05 parallel fields observed while ACS was observing the NICP fields. The numbers are referenced throughout the paper as Regions 1-5.

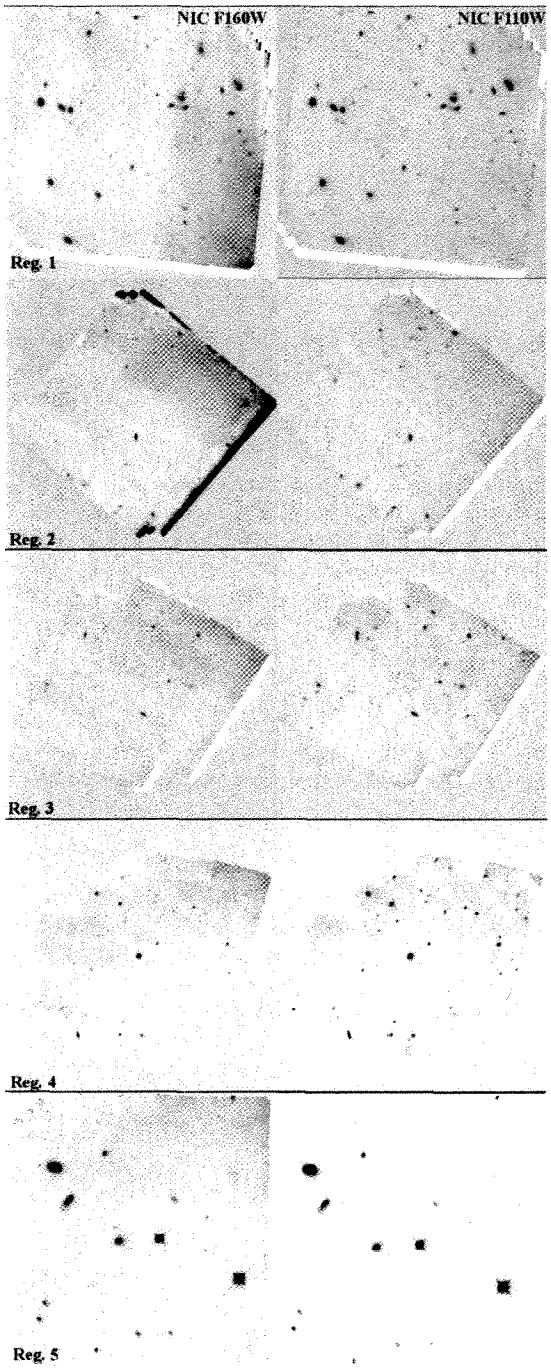

Fig. 2.— UDF05 NICMOS detection images. The ten images display the five UDF05 NICMOS parallel fields after data reduction and drizzling processes. The left panels show the F110W filter and the right panels show the F160W filter. Regions 1-5 are labeled for each set.

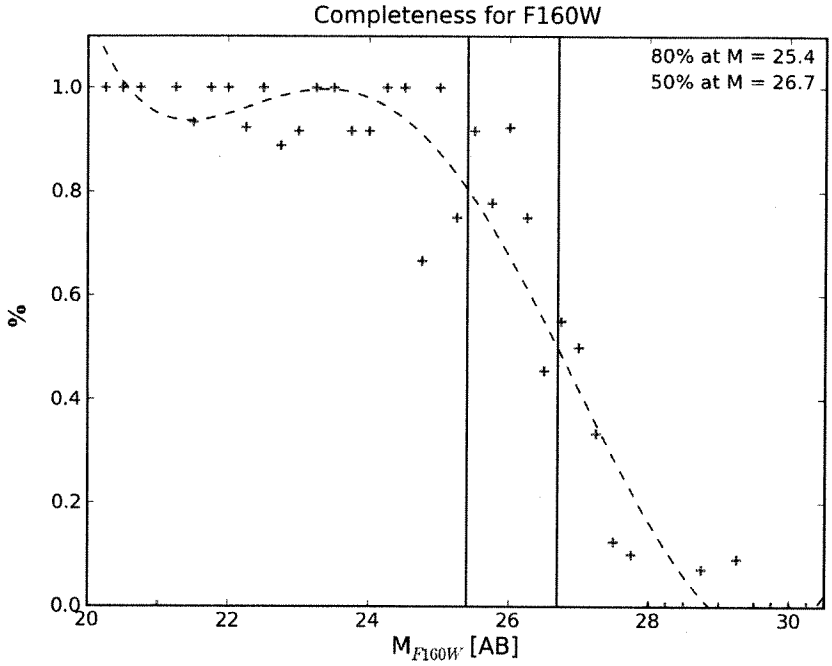

Fig. 3.— Detection Completeness for NICMOS F160W. The data are the detection ratio at magnitude (M_{AB}) for the NICMOS H_{160}-band along with a polynomial fit (dashed line). Completeness at 80% and 50% are listed in the upper right corner and are also marked with the vertical lines.

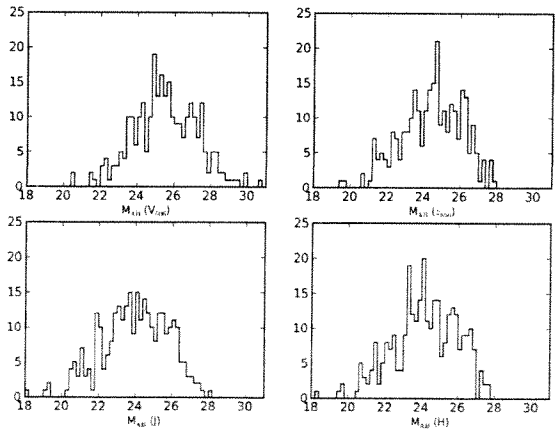

Fig. 4.— Magnitude histograms. The M_{AB} distributions for the real data sample in the ACS V_{606} and z_{850} filters (top), and for the two NICMOS J_{110} and H_{160} filters (bottom).

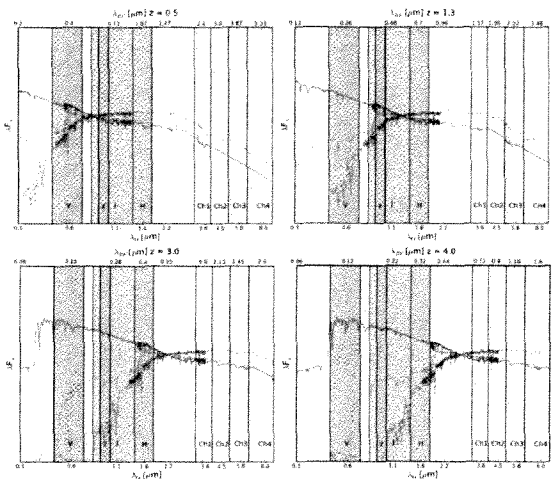

Fig. 5.— Simple stellar population templates for a galaxy with solar metallicity and evolved to three different ages: 5 Myr (blue solid line), 290 Myr (green dash-dotted line), and 1.4 Gyr (red dashed line). The four plots show the spectral lines redshifted for $z = 0.5, 1.3, 3.0,$ and4.0 as labeled. Rest-frame wavelengths (λ_{RF}) are labeled along the top axis, corresponding with the labeled observed wavelength (λ_O) along the bottom axis; note that the wavelengths are logscale to embellish the spectral features, particularly the Balmer-break feature, for clarity. The bandwidths for the ACS V_{606}, z_{850}, NICMOS J_{110}, H_{160}, and IRAC ch1, ch2, ch3, and ch4 filters are shown in the shaded regions. Note the redshifting of the Balmer-break at $\lambda_{RF} = 3646$ Å (0.3646μm). The templates are part of the BC03 model libraries and have exponentially decaying star formation.

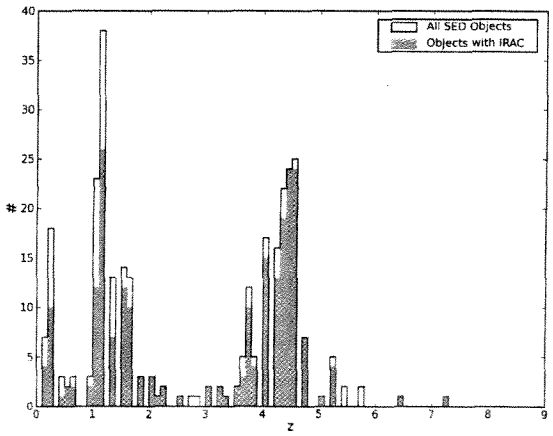

Fig. 6.— Distribution of photometric redshifts. The $z_{\rm phot}$ based on the results of the SED fitting for all 301 objects (black line), and the 231 objects with IRAC photometry (grey filled) show peaks at particular redshifts.

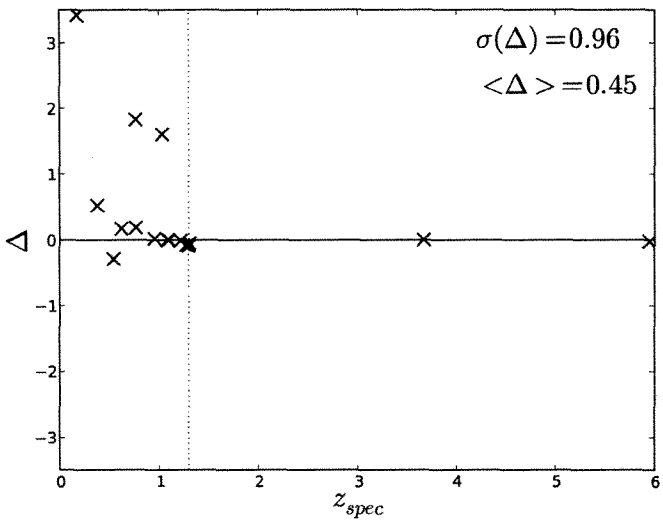

Fig. 7.— Comparison of $z_{\rm phot}$ and $z_{\rm spec}$. The data show the fractional error Δ as a function of $z_{\rm spec}$. The rms scatter σ and average error $< \Delta >= (z_{\rm phot} - z_{\rm spec})/(1 + z_{\rm spec})$ are listed in the top right corner. We determine that objects at $z > 1.3$ are much more likely to be correctly measured than at lower redshifts, because of the bandwidth coverage (or lack thereof) in the dataset (see Figure 5).

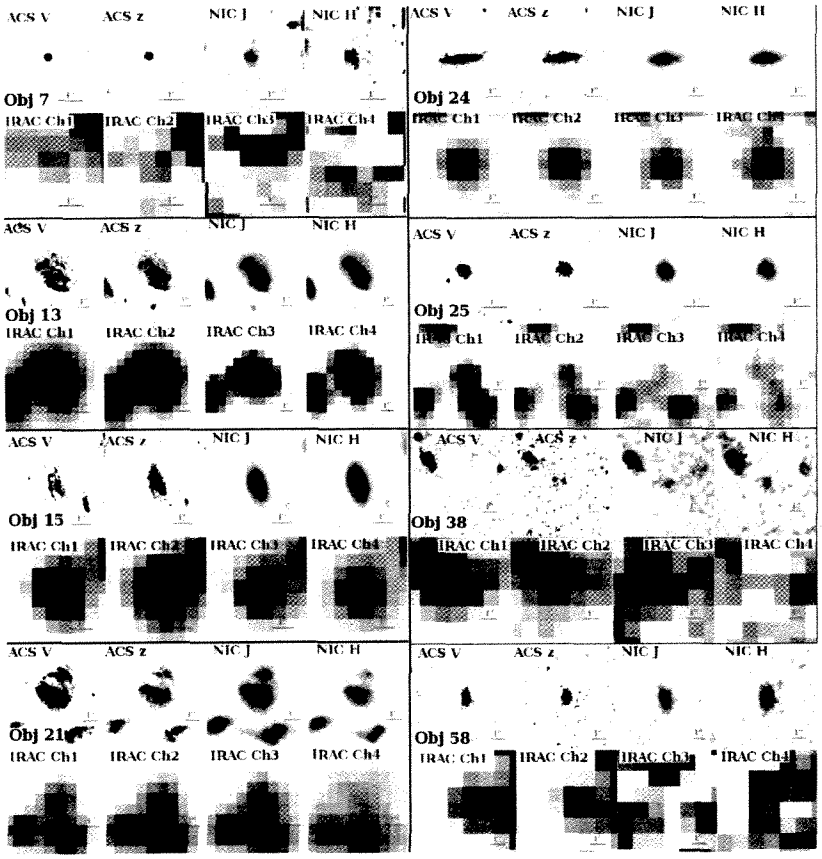

Fig. 8.— The 8 postage stamp panels for spectroscopically confirmed objects display the separate filter images for the V_{606}, z_{850}, J_{110}, H_{160}, and IRAC channels 1-4 as labeled. Note the 1″ ruler on each image for scale comparisons.

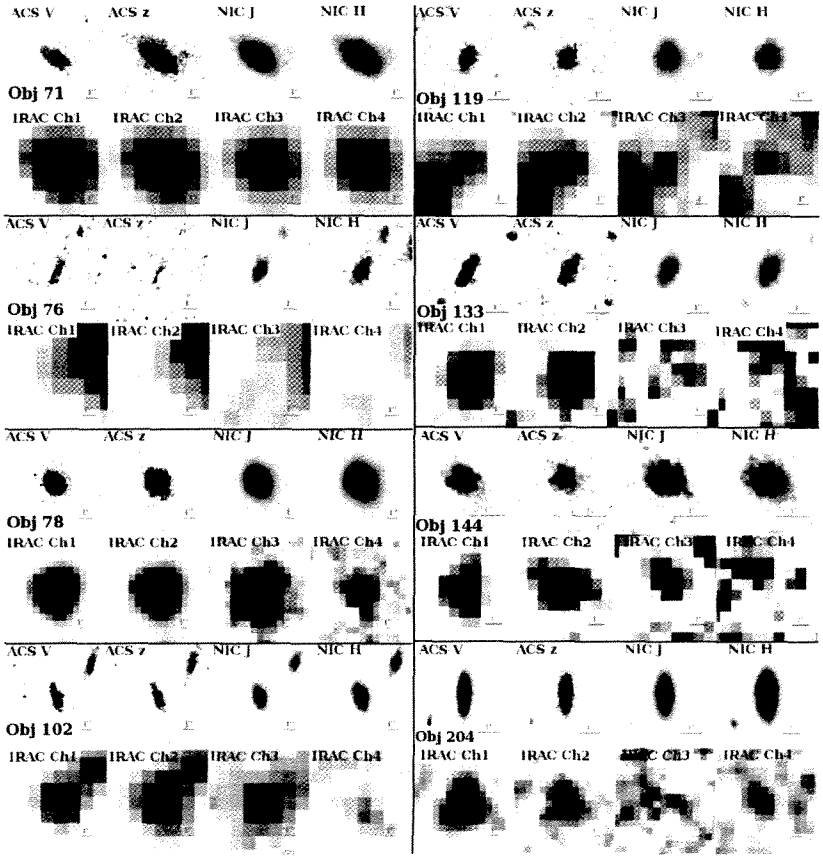

Fig. 9.— See Figure 8

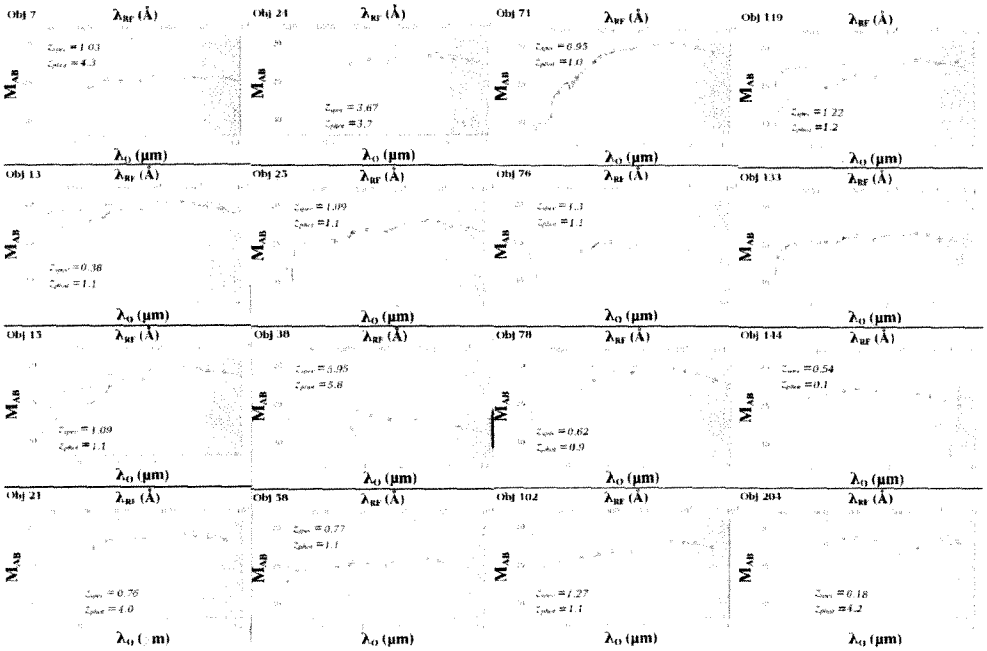

Fig. 10.— The best-fit SEDs for spectroscopically confirmed objects. Included in each plot are the photometric and spectroscopic redshift values. See Table 3 for the calculated SED parameters. The blue/red line is the flux with/without dust (see online version for color plots).

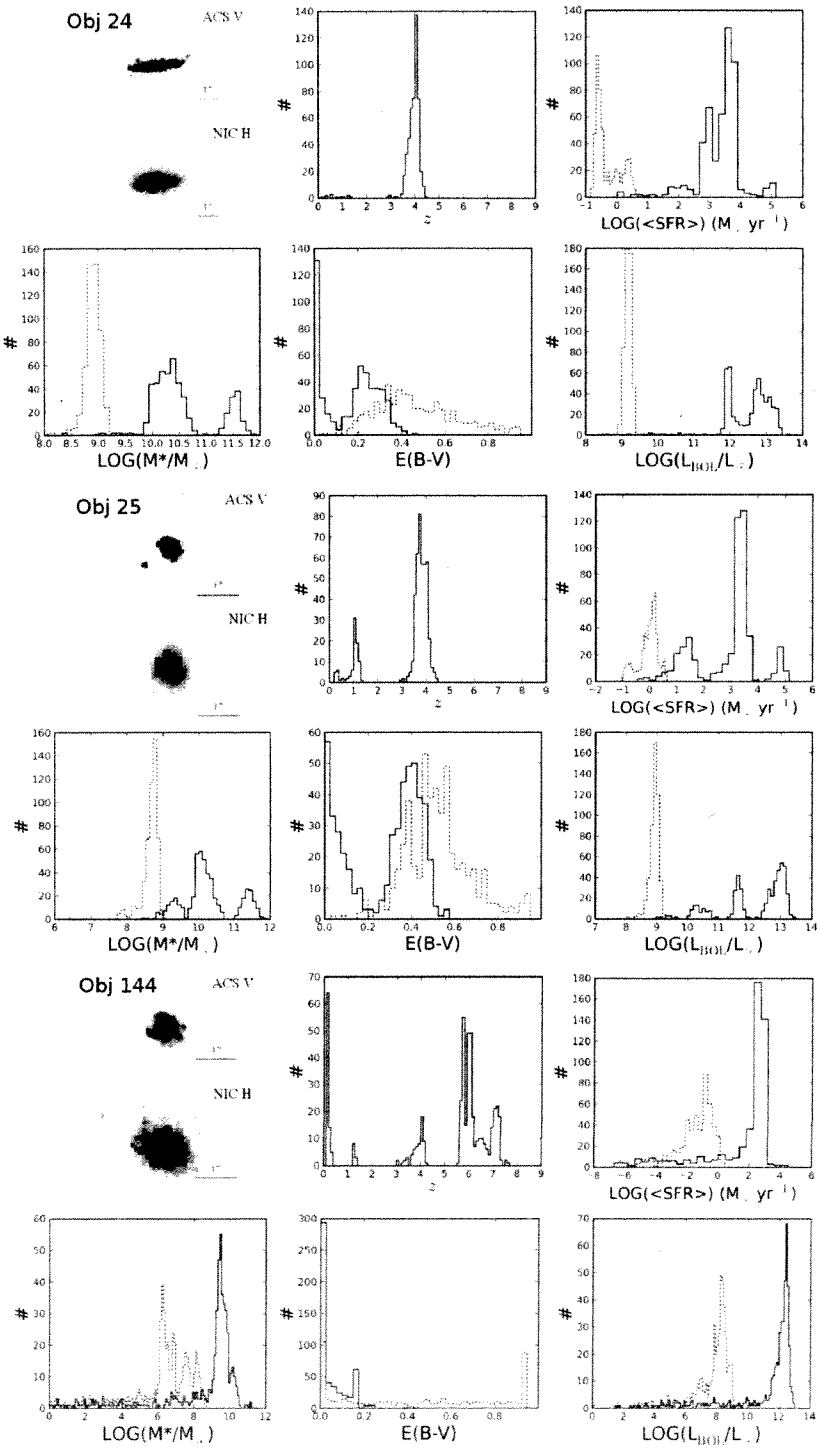

Fig. 11.— Monte Carlo simulation results for Objects 24, 25, and 144. The five Histograms show different SED parameters determined from random resampling through Monte Carlo simulations. The parameters are from left to right: redshift, average star formation rate, log(M*), E_{B-V}, and log(L_{Bol}) (no dust). The dotted line shows the results based a constant z_{phot}.

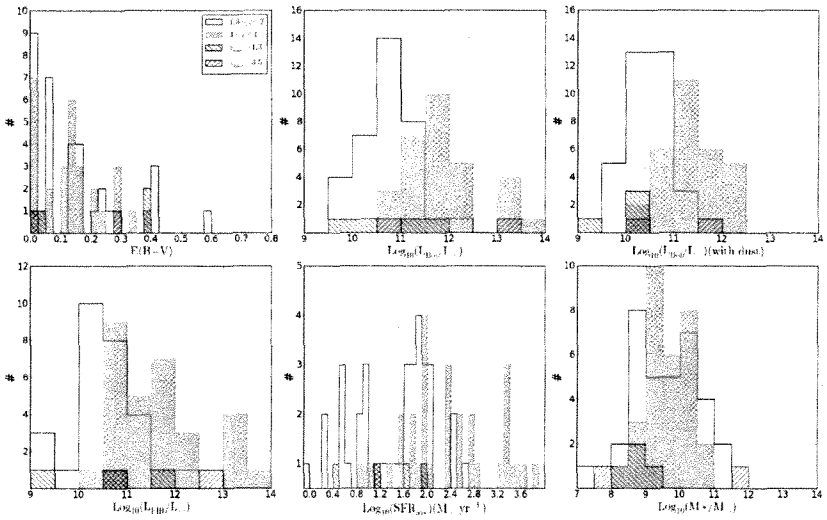

Fig. 12.— SED parameters for redshift-selected galaxies. From left to right, E_{B-V}, L_{Bol} (without and with dust extinction), L_{FIR}, average SFR and M* are plotted for galaxies in the redshift ranges: $1.3 \leq z \leq 2$ (35 objects) and $3 \leq z \leq 4$ (31 objects). The diagonally hatched bars indicate galaxies with spectroscopic redshifts at $1.2 \leq z \leq 2$ (objects 76, 102, 119, and 133) and $z > 3$ (objects 24 and 38).

TABLE 1
EXPOSURE PROPERTIES OF THE UDF05 NICMOS PARALLEL FIELDS

Region	t_{exp} sec	# Images	Area arcmin^2
1	52158	40	0.95
2	17919	14	1.32
3	15359	12	1.23
4	23039	18	1.72
5	60157	47	0.86

TABLE 2
SOURCE EXTRACTION PARAMETERS USED FOR THE NICMOS CATALOG

Parameter	Value
DETECT_MINAREA	16
THRESH_TYPE	RELATIVE
ANALYSIS_THRESH	1.2
DEBLEND_NTHRESH	32
DEBLEND_MINCONT	.005
WEIGHT_TYPE	WEIGHT_MAP
WEIGHT_IMAGE	mask.fits, weightmap.fits
FILTER_NAME	gauss_1.5_3x3.conv

TABLE 3

BEST FIT SED PARAMETERS FOR OBJECTS WITH SPECTROSCOPIC REDSHIFTS

Object	z_{spec}	z_{phot}	E_{B-V}	t_{SB} Gyr	τ Gyr	Z $Z_\odot$	log(L_{Bol}) $L_\odot$	log(L_{FIR}) $L_\odot$	log(M^*) $M_\odot$	M/L $M_\odot\ L_\odot^{-1}$	SFR_1[a] $M_\odot\ yr^{-1}$	SFR_2[a] $M_\odot\ yr^{-1}$	SFR_{ave} $M_\odot\ yr^{-1}$	χ^2
7[d]	1.03	4.3	0.075	0.10	0.8	0.2	11.05	11.25	9.33	0.007	20	22	21	4.05
13[b]	0.38	1.1	0.225	0.05	0.0	2.5	11.22	11.47	10.27	0.040	286	472	371	2.40
15*[d]	1.09	1.1	0.3	0.29	0.0	1	10.83	10.85	10.39	0.178	15	261	86	3.41
21[c]	0.76	4.0	0.275	0.01	0.0	0.2	12.26	13.31	12.02	0.048	> 5000	> 5000	> 5000	3.62
24*[b]	3.67	3.7	0.3	0.01	0.0	0.2	11.88	13.00	11.71	0.048	> 5000	> 5000	> 5000	5.21
25*[d]	1.09	1.1	0.05	0.10	0.0	2.5	10.28	9.58	9.23	0.075	10	27	17	3.74
38*[d]	5.95	5.8	0.0	0.01	1.0	0.2	10.44	10.58	7.82	0.001	13	13	13	18.48
58*[d]	0.77	1.1	0.0	0.05	0.0	2.5	9.89	7.09	8.49	0.040	5	8	6	21.46
71*[b]	0.95	1.0	0.025	1.02	0.0	1	11.12	9.86	10.75	0.408	0	565	56	5.51
76*[d]	1.30	1.1	0.0	0.10	0.0	0.4	9.42	8.96	8.43	0.075	2	4	3	18.78
78*[b]	0.62	0.9	0.325	0.10	0.0	0.2	10.85	11.38	11.18	0.489	875	2403	1512	7.75
102*[b]	1.27	1.1	0.375	0.01	1.0	2.5	10.39	11.51	8.68	0.001	48	49	48	3.05
119*[d]	1.22	1.2	0.375	0.03	0.0	2.5	10.38	10.94	9.45	0.025	80	108	94	12.43
133*[d]	1.31	1.2	0.025	0.05	0.0	2.5	10.14	9.33	8.81	0.040	10	16	13	3.50
144[b]	0.54	0.1	0.0	0.72	0.2	0.2	8.07	6.68	7.07	0.098	0.002	0.06	0.02	1.70
204[b]	0.18	4.2	0.0	0.01	1.0	2.5	12.27	11.88	9.57	0.001	366	369	368	9.67

*These objects have $|\Delta| < 0.2$

[a] SFR_1 is calculated at the age $t = t_{sb}$; SFR_2 is calculated at the age $t = 0$.

[b] z_{spec} were obtained from the VVDS CDF-S (Le Fevre et al. 2004)

[c] z_{spec} were obtained from Szokoly et al. (2004)

[d] z_{spec} were obtained from the GOODS VLT FORS2 survey (Vanzella et al. 2006).

TABLE 4

PARAMETER VALUES FROM MONTE CARLO SIMULATIONS

Object	z_{mc} [a]	z_{phot} [b]	Percentage [c] z_{phot}	$< E_{B-V} >$ [d]	Z ($Z_\odot$)	L_{Bol} ($L_\odot$)	M* ($M_\odot$)	$< SFR_{ave} >$ [d] ($M_\odot$ yr^{-1})	$< t_{sb} >$ [d] (Gyr)
7	4.2	4.3	12.0	0.04	0.2	11.2	8.2	103	0.42
	1.0	–	–	0.145	0.2	7.8	7.6	1	1.93
13	4.0	1.1	0.0	0.27	1	14.1	11.1	> 5000	0.06
	0.3	–	–	0.821	0.2	9.2	8.9	1	2.04
15	1.0	1.1	11.2	0.36	2.5	10.8	10.3	> 5000	0.59
	1.0	–	–	0.901	0.2	9.6	9.4	6	1.03
21	4.1	4.0	24.2	0.19	0.2	13.4	10.4	> 5000	0.04
	0.8	–	–	0.551	0.2	9.5	9.1	1	2.47
24	4.0	3.7	9.0	0.16	0.2	11.8	10.3	> 5000	0.05
	3.6	–	–	0.461	0.2	9.1	8.9	1	2.03
25	3.8	1.1	3.6	0.27	0.2	13.0	10.1	> 5000	0.15
	1.0	–	–	0.518	0.2	8.9	8.7	1.2	0.72
38	5.7	5.8	16.4	0.01	0.2	10.7	7.7	18	0.02
	5.8	–	–	0.402	0.2	6.5	6.4	0.03	0.52
58	4.0	1.1	1.6	0.06	0.2	11.2	9.3	272	0.13
	0.8	–	–	0.144	0.2	8.0	7.8	0.10	1.61
71	0.8	1.0	4.8	0.21	1	10.9	10.6	> 5000	1.2
	1.0	–	–	0.818	0.2	9.9	9.6	3	2.38
76	4.0	1.1	5.8	0.07	2.5	10.9	8.1	65	0.12
	1.2	–	–	0.181	0.2	7.0	6.9	0.2	1.09
78	4.4	0.9	1.0	0.26	1	13.7	10.7	> 5000	0.46
	0.6	–	–	0.609	0.4	9.6	9.3	1	2.87
102	3.5	1.1	0.6	0.18	0.2	11.7	11.3	> 5000	0.20
	1.2	–	–	0.639	0.2	8.4	8.2	0.2	0.82
119	3.6	1.2	6.6	0.24	0.2	11.7	10.8	> 5000	0.46
	1.2	–	–	0.693	0.2	8.4	8.2	0.3	0.52
133	0.1	1.2	3.0	0.07	1	11.2	9.4	498	0.09
	1.2	–	–	0.207	0.2	7.6	7.3	0.1	0.85
144	5.7	0.1	10.5	0.04	0.4	12.5	9.3	532	0.02
	0.5	–	–	0.449	2.5	8.2	6.2	0.2	0.77
204	6.0	4.2	0.0	0.02	2.5	12.4	10.4	1805	0.02
	0.2	–	–	0.833	2.5	9.3	7.1	1	0.69

[a] z_{mc} is the peak value of the redshift in the Monte Carlo simulations.

[b] z_{phot} is the best-fit redshift measured from SED fitting.

[c] The percentage of Monte Carlo simulations that resulted in the z_{phot} value.

[d] $< E_{B-V} >$, $< SFR_{ave} >$ and $< t_{sb} >$ are mean values.